# Real-time acoustic emission monitoring of wear-out failure in SiC power electronic devices during power cycling tests

Chanyang Choe, *Student Member, IEEE*, Chuantong Chen, *Member, IEEE*, Shijo Nagao, *Member, IEEE*, Katsuaki Suganuma, *Fellow, IEEE*

***Abstract*- In the study, acoustic emission (AE) was applied to monitor the wear-out failure in discrete SiC Schottky barrier diodes (SBD) devices with a Ag sinter die attach to successfully monitor the real-time progress of failure of Al ribbons for the first time. After eliminating background AE noise including the power on-off switch and the ambient noise via a noise filtering process, AE signals were successfully collected for the SiC devices during a power cycling test. Furthermore, AE monitoring was compared to the traditional failure monitoring method using forward voltage. Physics-of-Failure (POF) analysis was performed, and fatigue cracks and lift-off in Al ribbons were confirmed as the dominant failure modes for the discrete devices. Specifically, AE counts that correspond to one of the time-domain parameters of AE signals increased with power cycling, thereby corresponding to the observed fatigue cracks in Al ribbons leading to lift-off failure. Additionally, the AE count rate was highly correlated with the crack growth rate. Based on the relationship between an AE count rate and fatigue crack growth rate, the results indicate that AE monitoring can be used to understand the fatigue propagation in Al ribbons (i.e., failure mechanism) and also as an early warning before catastrophic lift-off fracture for power electronic devices.**

***Index Terms*- Acoustic emission (AE), Al ribbon, Failure, Monitoring, Power cycling test (PCT), Ag sinter joint**

## I. Introduction

Power electronic devices are widely used for energy conversion in various industries such as electric vehicles, power generation, and renewable energy. The emergence of power electronic devices using silicon carbide (SiC) semiconductors has facilitated more compact designs and high energy efficiency due to its superior material properties [1]–[3]. However, compared to traditional silicon (Si), the raised energy density of SiC-based power electronic devices requires high-temperature operation and results in many reliability issues [4]–[6].

This work was supported by the JST Advanced Low Carbon Technology Research and Development Program (ALCA) project "Development of a high frequency GaN power module package technology" (Grant No. JPMJAL1610) and based on results obtained from a project (JPNP14004) commissioned by the New Energy and Industrial Technology Development Organization (NEDO). *(Corresponding author: Chuantong Chen.)*

C. Choe, C. Chen, S. Nagao, K. Suganuma, are with Institute of Scientific and Industrial Research, Osaka University, Mihogaoka 8-1, Ibaraki, Osaka 567-0047, Japan. (Email: chenchuantong@sanken.osaka-u.ac.jp).

In SiC-based power electronic devices, wear-out failure after long-term operation is mainly caused by the failure in packaging components, such as bond wire lift-off, substrate delamination and die attach cracks, because the existing packaging components based on Si devices are not durable enough to satisfy strict reliability requirements [6][7][8].

Generally, the wear-out failure of power electronics devices is evaluated by Physics-of-Failure (POF) analysis after a power cycling test (PCT) or thermal shock test (TST) [9][10][11]. However, the POF analysis is much complex and expensive for application in field reliability and it cannot predict the lifetime of power electronics. Recently, many studies focused on real-time monitoring methods using various failure precursor parameters, which make it possible to analyze the wear-out failure mechanism and lifetime during a reliability test. The value of failure precursor parameters, such as ON-state resistance, collector-emitter voltage, forward voltage, junction temperature, and thermal resistance, are well related and change with the wear-out failure of packaging components during device operation, and thus provide information for the final failure [12][13]. However, the current failure precursor monitoring is limited for application in power electronic devices [14] because it requires an additional electric circuit and high-resolution measurement to sense a small deviation under a high-voltage high-current operation [15]. Additionally, failure precursor parameters are sensitive to final failure although they are unable to detect failure progress [16]. Finally, the variation in one of the failure precursor parameters can affect another parameter, which results in an incorrect understanding of wear-out damage mechanism and lifetime prediction [17][18]. Therefore, it is necessary to modify failure precursor monitoring.

Acoustic emission (AE) monitoring is used as a real-time evaluation technique for material damage in bulk materials [19] and various microelectronics such as lithium-ion batteries [20], multi-layered ceramic capacitors [21], and fuel cells [22]. An AE sensor is attached to the test object and detects the elastic waves released from materials when they are damaged during a reliability test. The damage includes cracking, delamination, and fracture. Fig. 1 shows an example of the occurrence and propagation process of elastic waves from the wear-out failure of power electronic devices. The elastic waves detected due to

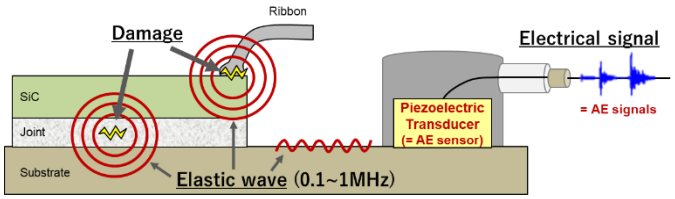


Fig. 1 Generation, propagation, and collection process of acoustic emission signals (i.e., elastic waves) in power electronics during PCT.

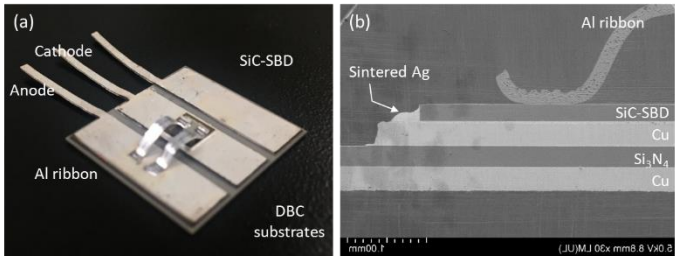


Fig. 2 Fabricated discrete SiC-SBD devices; (a) optical image and (b) cross-section SEM image.

damage is termed as AE signals and include various damage information such as the amount, size, and growth ratio of damage. Damage and final failure information is defined via analyzing time-domain and frequency-domain characteristics of AE signals including counts, amplitude, and a central frequency. Recently, Karkkain et al. attempted to use an AE sensor on a half-bride power module that consists of power semiconductors, capacitor, and inductors during PCT [23]. Although AE signals were collected during power module switch, it was not possible to confirm whether the AE signals were released from wear-out failure or simply generated from the power on-off switch. Therefore, the relationship between collected AE signals and damage should be confirmed to apply AE to monitor the wear-out failure of power electronic devices. Additionally, for accurate AE assessment, background AE noise, such as the power on-off switch noise and ambient noise, should be filtered during PCT.

In the study, AE was applied for the first time to real-time monitoring of wear-out failure of discrete SiC Schottky barrier diode (SiC-SBD) devices during PCT. In section II, the structure of discrete SiC-SBD devices, PCT setups, and a real-time AE monitoring system is explained. Section III details the monitoring of forward voltage of discrete devices during power cycling. The Physics-of-Failure (POF) analysis of tested power discrete devices was performed via field emission scanning electron microscopy (FE-SEM) and X-ray inspections. Section IV describes the filtering of background AE noise via the noise filtering process for accurate AE assessment. Furthermore, the collection of AE signals during PCT and relationship between the observed damage and acquired AE signals is presented. Finally, the performance of the proposed real-time AE monitoring is demonstrated based on the relationship.

## II. EXPERIMENT

### *A. Tested Discrete Devices*

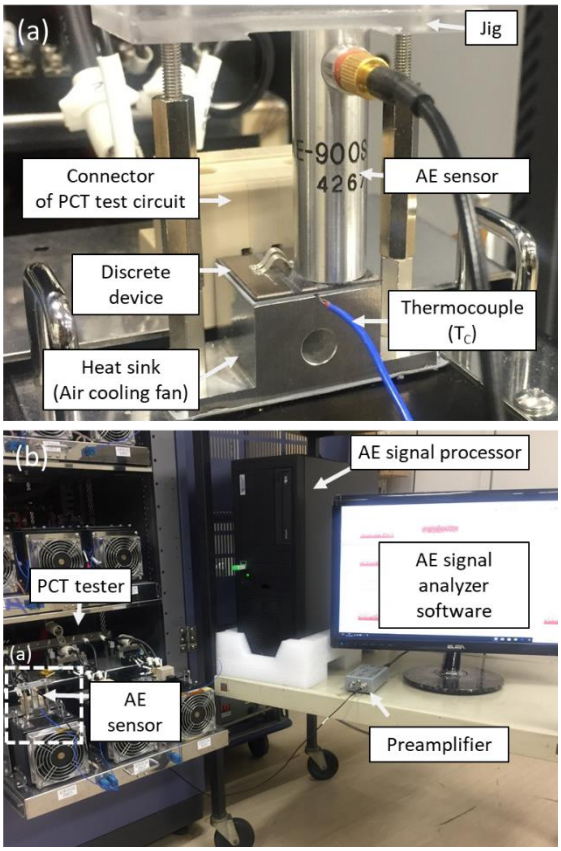


Fig. 3 (a) Experimental apparatus for PCT and real-time AE monitoring and (b) configuration of an AE system.

Power semiconductors, such as MOSFETs, IGBTs, and diodes are commonly packaged in two types of structures such as discrete devices and power electronic modules. When compared with modules, discrete devices exhibit a simpler packaging structure including one power semiconductor, a substrate, die-attachment (i.e. joints), and wire interconnection. In the study, with respect to the first attempt of AE monitoring, a discrete device with a simpler packaging structure was used. Fig. 2 shows the tested discrete device. The device was fabricated using one 1200 V/50 A SiC Schottky barrier diode (SBD) with a dimension corresponding to 4.77 mm × 4.77 mm × 0.235 mm. The SiC-SBD device was die attached on an active metal brazing (AMB) substrate by using a micron Ag sinter paste and was interconnected via Al ribbons. The AMB consisted of a $Si_3N_4$ ceramic plate of 0.32 mm thickness and two Cu metallized layers with 0.30 mm thickness. Among the three types of ceramic including $Al_2O_3$, AlN, and $Si_3N_4$ in AMB substrates, the $Si_3N_4$ based AMB substrate was selected because it exhibited the highest thermal damage resistance [24][25]. To focus on failure monitoring of Al ribbons in the discrete device, micron Ag sinter paste [26] was selected as the die attach material because it exhibited a higher thermal resistance when compared to that of traditional high-temperature solder [8], [27], [28]. With respect to Ag sinter joints, the backside of the SBD device and top side of AMB substrates were metallized with a 100-nm Ti barrier layer and 2-μm Ag adhesion layer in order. The Ag paste was printed on the AMB substrates with a

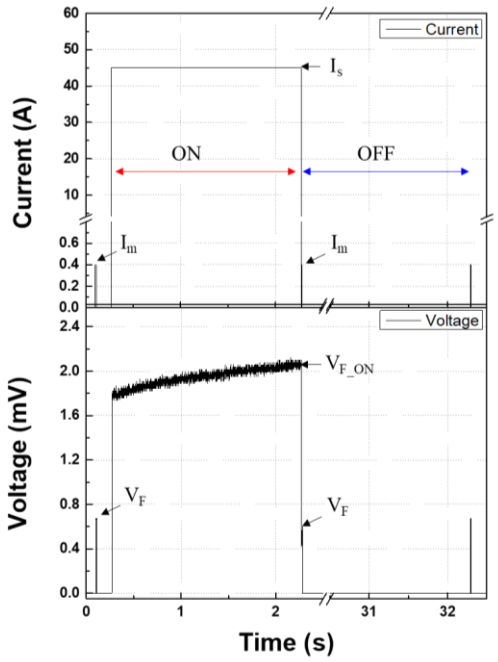


Fig. 4 Profiles of voltage and current during a power cycling test.

thickness of 100 μm via a stainless screen mask. The devices were placed onto the printed paste and heated at 250 °C for 1 h without sintering pressure. Subsequently, two Al ribbons with a cross-section area of 1.5 × 0.2 mm$^2$ were bonded on the SiC-SBD device and Cu layer of an AMB substrate using an ultrasonic ribbon bonder (HB-30, TPT Co.) with ultrasonic power corresponding to 20 W for 2 s [29].

*B. Power Cycling Test System and Setup*

PCT was performed using a power cycle test system (PST-2404, ESPEC Co.) and consisted of a power supply, switching circuit, $V_F$ measurement circuit, heatsink, and an air cooling system. The discrete device is mounted on the heatsink as shown in Fig. 3(a). A 50-μm thick silicon film was placed between the modules and heatsink to decrease interfacial thermal resistance. The heatsink was cooled via a rotating fan, and the temperature was maintained at approximately 25 °C.

During PCT, the discrete device is heated by a constant stress current (Is) corresponding to 45 A, as shown in Fig. 4. The heating ON time and OFF time were fixed at 2 s and 30 s, respectively, and performed an initial junction temperature swing ($\Delta T_j$) of 150 °C. The PCT condition is listed in Table 1. The harsh temperature swing was selected for the accelerated PCT test, and this exceeded the general $T_j$ of 100 °C [30]. Before and after the application of the stress current, the junction temperature ($T_j$) was measured via temperature dependent forward voltage ($V_F$). The value of $T_j$ is calculated as follows:

$$T_j = KV_F + m. \quad (1)$$

where $V_F$ was measured under low measurement current ($I_m$) corresponding to 400 mA, K denotes the linear association

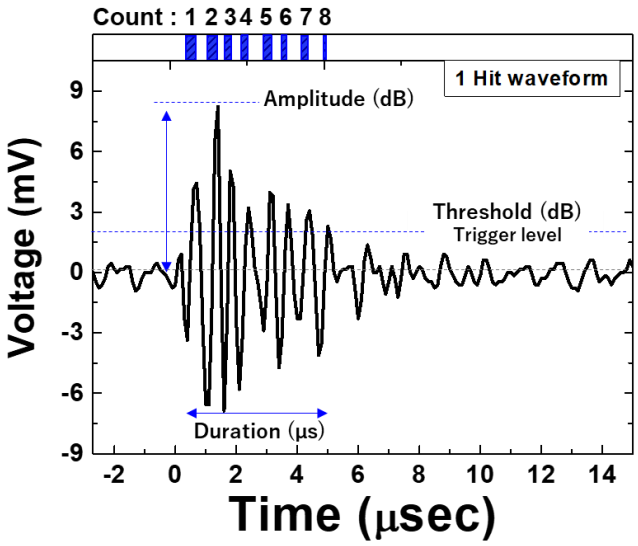


Fig. 5 Waveform of a collected AE signal and its characteristic including counts and amplitude.

TABLE I
CONDITION OF THE POWER CYCLING TEST.

| Stress current ($I_s$) | Stress time (s) | Measurement Current ($I_m$) | Cooling time (s) | Minimum junction temperature ($T_{j\_min}$) | Maximum junction temperature ($T_{j\_max}$) | Temperature Swing ($\Delta T_j$) | PCT cycles (N) |
|---|---|---|---|---|---|---|---|
| 45A | 2 s | 0.4 A | 30 s | 25 ℃ | 175 ℃ | 150 ℃ | 5,123 |

constant between $V_F$ and $T_j$, which is referred to as K-factor [31], and m denotes the material constant. Specifically, K and m were calculated by measuring $V_F$ at several different temperatures ranging from 25 °C to 200 °C.

During PCT, $V_{F\_ON}$ and $T_j$ were recorded at each cycle and monitored as failure precursor parameters. This is established as a good indicator to detect wear-out failure in bond-wire and die-attachment [14]. The temperature swing was repeated up to failure based on the failure criteria, which was defined as an increase in the $V_F$ by 20 % when compared to its initial value to protect the tested discrete devices against catastrophic failure [32].

*C. Acoustic Emission Monitoring System and Setup*

In the study, AE monitoring was proposed as a new wear-out failure monitoring method. During PCT, AE signals were detected from discrete devices and used to monitor the progress of failure. As shown in Fig. 3(a), the experimental apparatus is specially designed to simultaneously detect AE signals during PCT. Thus, AE signals were collected via a wideband piezoelectric AE sensor (AE-900S-WB, NF Electronics Co.), which was directly mounted onto the AMB substrate in discrete devices via an ultrasonic couplant and acrylic jig. The AE sensor was electrically insulated from the AMB substrate via an insulating ceramic layer on the bottom of the sensor. A wideband type sensor was selected for frequency analysis of the collected AE signals due to its high and uniform sensitivity with respect to a large frequency range from 100 kHz up to 1 MHz.

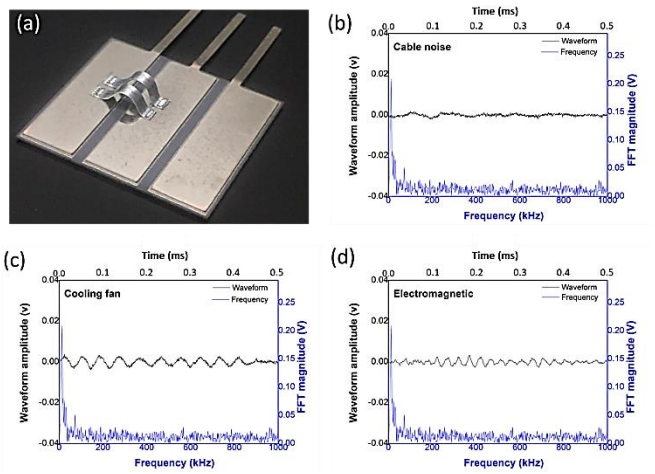


Fig. 6 (a) Dummy specimens designed for noise filtering and (b-d) Typical waveform and frequency spectrum of three types of collected noise; (b) cable noise, (c) cooling fan movement noise and (d) electromagnetic induction noise.

Because the frequency component of AE signals is strongly dependent with the resonant frequency of the used AE sensor, AE sensors with a large frequency range from 100 kHz up to 1 MHz was used in this study, which have some functions to avoid the resonance frequency influence. The collected AE signals were amplified via a preamplifier (2/4/6, Physical Acoustic Co.) at a gain of 40 dB and were filtered by analog high-pass filter (HPF) and low-pass filter (LPF). HPF is 4th order butterworth filter. Its filtering level can be selected to 1 kHz, 20 kHz, 100 kHz, and 200 kHz. LPF is 6th order butterworth filter. Its level also is selectable to 100 kHz, 200 kHz, 400 kHz, 1 MHz, 2 MHz, and 3 MHz. The filtering frequency level was decided based on the results of noise leveling test as mentioned in the next sub-section D of section II. The signals were recorded at a sampling rate corresponding to 2 MHz by the AE acquisition system (PCI-2, Physical Acoustic Co.), as shown in Fig. 3(b). The frequency filter has been reported in previous studies for the AE sensor applications [33] [34].

The characteristics of the AE signals were used to evaluate damage in the material. Fig. 5 shows the representative waveform of AE signals and its time-domain characteristic parameters [20]. The highest sound pressure is defined as amplitude. Essentially, a signal was recorded when its amplitude was higher than or equal to the threshold value, which corresponded to the criterion for effective signals. The number of times that a waveform exceeds the threshold is defined as AE counts and its time derivative. Additionally, the frequency-domain characteristics of AE signals were analyzed through Fast Fourier Transform (FFT). Specifically, FFT is commonly used to determine AE source in conjunction with time-domain parameters and also to eliminate noise.

*D. Background AE Noise Filtering Process and Setup*

Typically, the noise filtering method is applied to filter unnecessary noise and collect AE signals that correspond to the wear-out damage [35][36], which is considered as the most important step for accurate AE assessment. In noise filtering

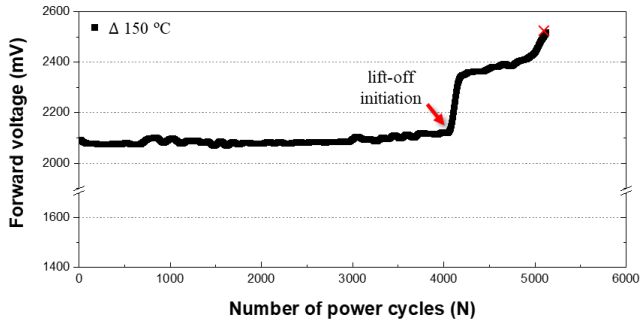


Fig. 7 Variation in forward voltage of a diode during PCT.

process, background noise must be collected under the same environment as that of an actual test and noise is filtered based on the investigated noise level including frequency. In the study, a noise levelling test was investigated using dummy specimens. The specimens were specially fabricated without the SiC-SBD chip and Ag sinter joints to avoid Joule heating of the diode. Patterned Cu islands on substrates are interconnected by Al ribbons, as shown in Fig. 6(a). Additionally, PCT was performed on the dummy specimens under the same condition including high current and fan cooling introduced in table 1. During PCT, all AE noise signals were recorded with the lowest level HPF of 1 kHz and with the highest level LPF of 3MHz to prevent the filter from removing or transforming noise and investigate the original frequency component of noise.

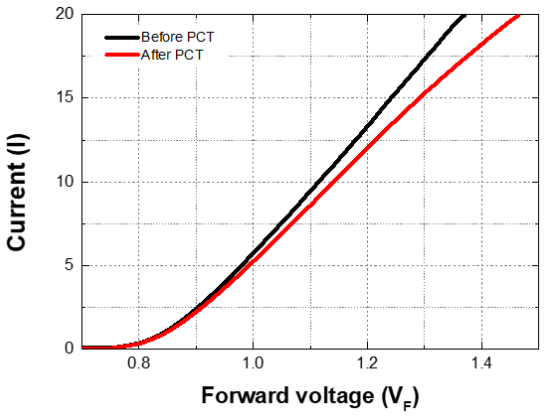


Fig. 8 I-V characteristics before and after PCT.

Figs. 6 (b), (c), and (d) show the representative surrounding noise signals from cables, a rotating fan, and switching on-off signals of high-current carrying circuits in the PCT system for the background AE noise filtering process, respectively. The recorded noise signals did not include AE signals from the damage of discrete devices because the used dummy specimen without a chip was not heated and damaged even under high current. The cables in AE system exhibited very low amplitude noise below 25 kHz. The mechanical vibration of a cooling fan (below 30 kHz) and the electromagnetic interference (EMI) of current switching (below 87 kHz) also generated noise signals. The frequency level of the collected AE noise ranged less than 87 kHz. Therefore, in order to more accurate signal measurement and meantime eliminate the noise, the high-pass frequency filter at 100 kHz was employed to eliminate noise in

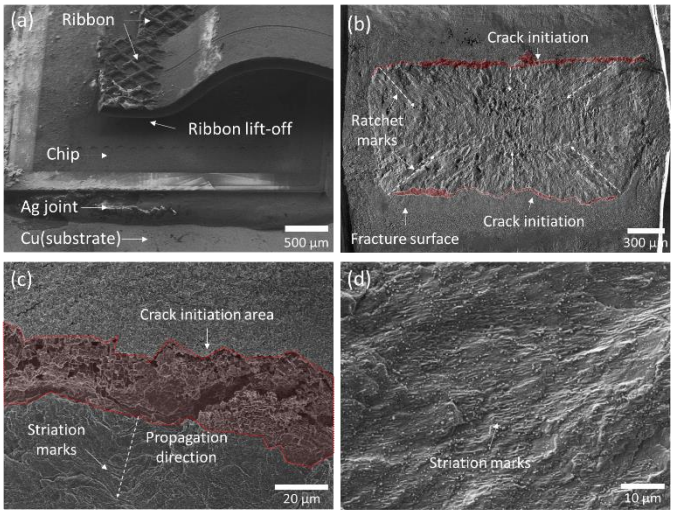


Fig. 9 Failure analysis results of failed discrete SiC-SBD devices after PCT; (a) lift-off failure of one Al ribbon, (b) fatigue fracture surface of lift-off ribbon, (c) magnified observation of crack initiation, and (d) magnified observation of fatigue fracture marks.

PCT and AE system for the SiC-SBD power module. Additionally, the threshold of 30 dB was set to eliminate the existing noise signals based on the amplitude of noise signals (below 26 dB), which still collected in a retried noise levelling test with high-pass frequency filter of 100 kHz. Subsequently, the noise levelling test using dummy specimens was repeated with the aforementioned setup of the high-pass filter and threshold. AE signals were not detected and the absence of occurrence of AE signals during PCT clearly indicated that the noise filtering process completely eliminated background AE noise.

Additionally, most industrial machinery vibrations including that of motors and engines exhibit a characteristic frequency response below 10 kHz. Thus, the AE system can be used for various power electronics in industrial environments without the noise problem.

## III. POWER CYCLING TEST

### *A. Voltage Precursor Parameter Monitoring in PCT*

Fig. 7 shows the $V_F$ measurement results of discrete SiC-SBD devices during the power cycling test under the test condition as listed in Table 1. After 4,060 cycles, a sudden increase was observed in $V_F$, and this increased by 20 % from its initial value after 5,123 cycles. Lifetime of devices could be determined based on the failure criteria of a $V_F$ increase.

Fig. 8 shows a comparison of current–voltage (I–V) characteristics of discrete devices before and after PCT. The I-V curves were measured at room temperature via a curve tracer (CS-3200, IWATSU Co.). The electrical resistance ($R_F$) of the discrete devices was measured from I–V curves, and it was observed that it increased after PCT. The measured $R_F$ corresponds to the sum of individual resistances in chip and packaging and is simply expressed as follows:

$$R_F = R_{chip} + R_{packaging} \,. \qquad (2)$$

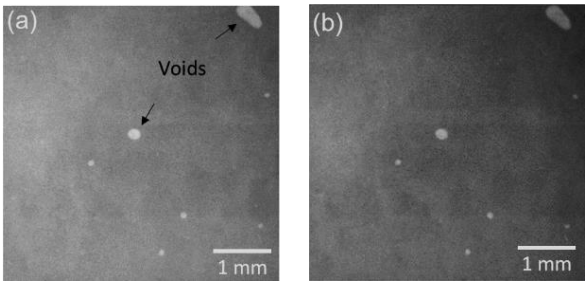


Fig. 10 Micro-focused X-ray inspection results of Ag sinter joints in discrete devices before PCT (a) and after PCT (b).

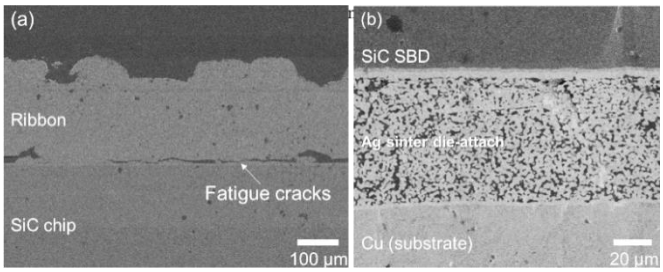


Fig. 11 Cross-section observation of (a) one unfeatured ribbon and (b) Ag sinter joint in the tested discrete SiC-SBD devices after PCT.

where $R_{chip}$ and $R_{packaging}$ denote the resistance of the chip and resistance of packaging elements including ribbons, die-attachment, metallization, and substrates, respectively. Generally, an increase in $R_{chip}$ occurs due to the oxidation of leads of Si diodes. In the case of SiC diodes, a significant change was not observed in the electrical characteristic up to a maximum exposure temperature of 240 °C [37]. On the other hand, failure in die-attachment and bond wire leads to a significant increase in $R_F$ after PCT with $\Delta T_j$ from 80 °C to 160 °C given the decrease in cross-section area in packaging elements acting as the current path, thereby leading to an increase in $R_{packaging}$ [38]. Therefore, $R_F$ increased after power cycling, and these results from failures such as cracks, delamination, and lift-off failure in die-attachment or in ribbon bonding. Additionally, $V_{F\_ON}$ variation shown in Fig. 7 is given as follows:

$$V_{F\_ON} = I_S \cdot R_F = I_S \cdot (R_{chip} + R_{packaging}) \,. \qquad (3)$$

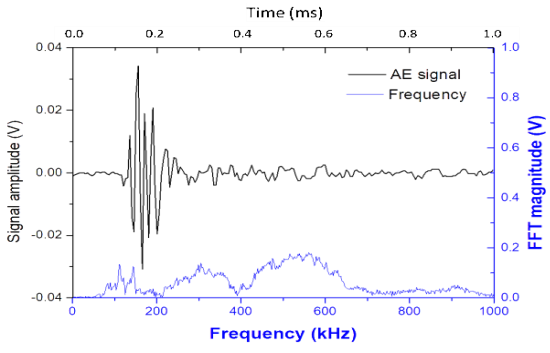


Fig. 12 Waveform and its corresponding frequency spectrum of typical AE signals collected during PCT.

where $I_S$ denotes the stress current for heating in power cycling test. In the study, $I_S$ was fixed at 45 A. In order to maintain the constant stress current, the increase in $R_F$ after PCT increases in $V_{F\_ON}$.

*B. Physics-of-Failure Analysis of Tested Discrete Devices*

The failure mode of tested discrete devices was evaluated via FE-SEM observation and X-ray transmission inspection. Figs. 9 show the inspection results of the appearance and fracture surface of devices after PCT. One of the two Al ribbons is completely fractured by lift-off and the other ribbon is still bonded on a chip, as shown in Fig. 9 (a). Ratchet marks are observed on the fracture surface of the ribbon lift-off as shown in Fig. 9 (b). The marks, which are typically observed on a fatigue fracture surface, indicated that the lift-off failure was induced by fatigue. Generally, fatigue fracture involves three steps including crack initiation, crack propagation, and final fracture. The sharp and large fatigue cracks initially occur at the edge of Al ribbon bonding as shown in Fig. 9 (c). There is a large cracked region between the spot marked 'crack initiation area' and the area containing striations. The cracks propagated

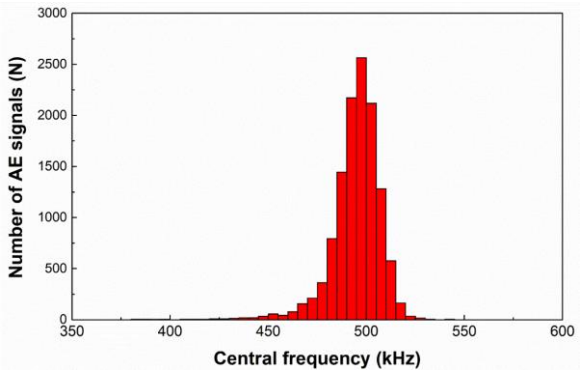


Fig. 13 Histogram of the measured central frequency of collected AE signals.

into the center in the direction of ratchet marks as shown in Fig. 9 (b), and this is followed by the final lift-off failure. Striation marks in the vertical direction to ratchet marks are observed as shown in the magnified images of Fig. 9 (d), and this also indicates the propagation direction of fatigue cracks. Fig. 10 shows the micro-focused X-ray inspection (XVA-160N, Uni-Hite System Corporation, Japan) results of Ag sinter joints in the discrete device before and after PCT. It is found that some small voids in the Ag sinter joint structure after sintering process as shown in Fig.10 (a). After the power cycling test, the voids almost did not any change as shown in Fig.10 (b). Hence, it can be inferred that the sinter Ag joined structure had an appropriate interface bonding ratio during the sintering process and high power cycling reliability. Although the thermal shock resistance of Ag sinter joints depends on manufacturing conditions, chip size, and the used Ag paste [39] [40] [41], the results in the present study indicate that Ag sinter joints exhibit excellent high temperature reliability for PCT.

Fig. 11 shows the cross-section of one unfractured ribbon of the tested discrete device after PCT. More than half of the bonded interface between an Al ribbon and a SiC-SBD chip is

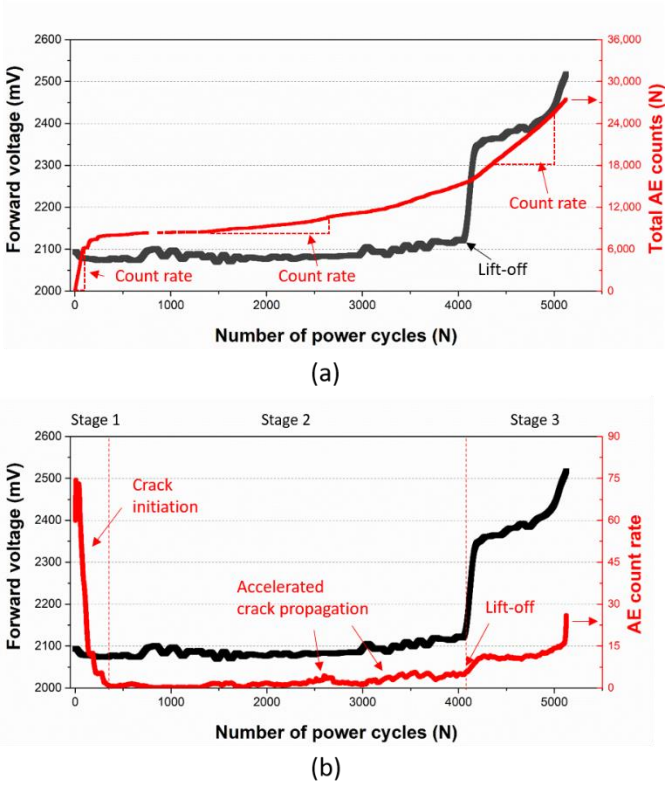


Fig. 14 Monitoring result of total AE counts (a) and AE count rate (b) during PCT with the monitoring results of forward voltage.

delaminated, and this is caused by fatigue cracks, as shown in Fig. 11 (a). Conversely, after PCT, any delamination did not occur at the interface between sintered Ag and the substrate or between sintered Ag and a SiC-SBD chip, as shown in Fig. 11 (b). The Ag sinter joints maintained a micro- porous network structure without any evident cracks, and this can be attributed to the robust die shear strength of approximately 40 MPa and a low resistivity of $3.9 \times 10^{-6}$ Ω cm [26].

Based on the results of Al ribbons and Ag sinter joints after PCT, fatigue cracks and lift-off in Al ribbons corresponded to the dominant failure modes in the discrete devices used in the current study. The results were similar to those reported in previous studies wherein bond wire lift-off corresponds to the main failure mechanism. The $V_F$ of diodes increases with the bond wire lift-off [42][43][44]. Therefore, Al ribbon's lift-off corresponds to the main reason for increases in $V_F$, as shown in Fig. 7, and it is evaluated via $V_F$ measurement. However, although the observed fatigue cracks gradually propagated before final lift-off failure, $V_F$ was not changed prior to the sudden increase that is caused by lift-off failure. In this case, the measurement of $V_{F\_ON}$ cannot be used to monitor the progress of fatigue cracks in the Al ribbon, and thereby resulting in the ribbon's final lift-off failure.

## IV. ACOUSTIC EMISSION MONITORING TEST

*A. Source of Acoustic Emission*

The AE monitoring was simultaneously performed with PCT and a number of AE signals were collected during PCT.

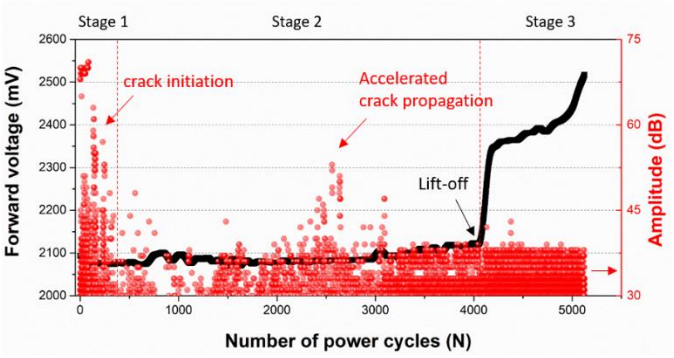


Fig. 15 Monitoring result of amplitude of collected AE signals during PCT with the monitoring results of forward voltage.

Fig. 12 shows typical waveform and their frequency spectrum. They indicate that the collected AE signals were burst type waveforms, and this was completely different when compared to the noise signals shown in Fig. 6. It is known that the burst type signals are typically emitted via a sudden energy release when damage such as cracks and delamination occurs [45]. Based on the typical source of burst type and the observed fatigue cracks in Al ribbon bonding shown in Fig. 9, the source of collected AE signals from discrete devices during PCT is attributed to fatigue cracks in the Al ribbon bonding.

The frequency components of collected AE signals are estimated by FFT, as shown in Fig. 12. They were also completely different with that of noise signal as shown in Fig. 6. These FFT results clearly prove that noise signals were completely filtered. The signals were composed of various frequency components. A central frequency, defined by the arithmetic mean of frequency components in the spectrum, was used to characterize the representative frequency of each AE signal [46]. Fig. 13 shows the distribution of estimated central frequency. It corresponds to a bell-shaped curve. A peak in the distribution curve was approximately 500 kHz. The frequency component depends on the type of fracture, which denotes the source mechanism of AE signals [47]. The bell-shaped distribution with a single peak also supports the fact that the collected AE signals are emitted simply from the fatigue cracks in Al ribbon bonding.

Frequency analysis of AE signal needs to be studied due to three reasons as follows; it relies heavily on FFT, which is a bit risky for a non-periodic signal such as the AE burst, it is slightly affected by the resonance characteristics of acoustic emission sensor, though its effect was minimalized by using wide-band sensor, and the usefulness of various calculation methods for the representative frequency needs to be compared and verified. Considering these, the frequency analysis method will be improved in the further work.

*B. Monitoring by Acoustic Emission Parameter*

Two types of time-domain characteristic parameters of collected AE signals including total AE counts and amplitude are monitored during PCT and are compared with $V_{F\_ON}$ monitoring results (Fig. 7), as shown in Fig. 14 and Fig 15, respectively. Fig. 14 (a) shows the monitoring results of total AE signal counts in PCT. The total number of AE counts (i.e.,

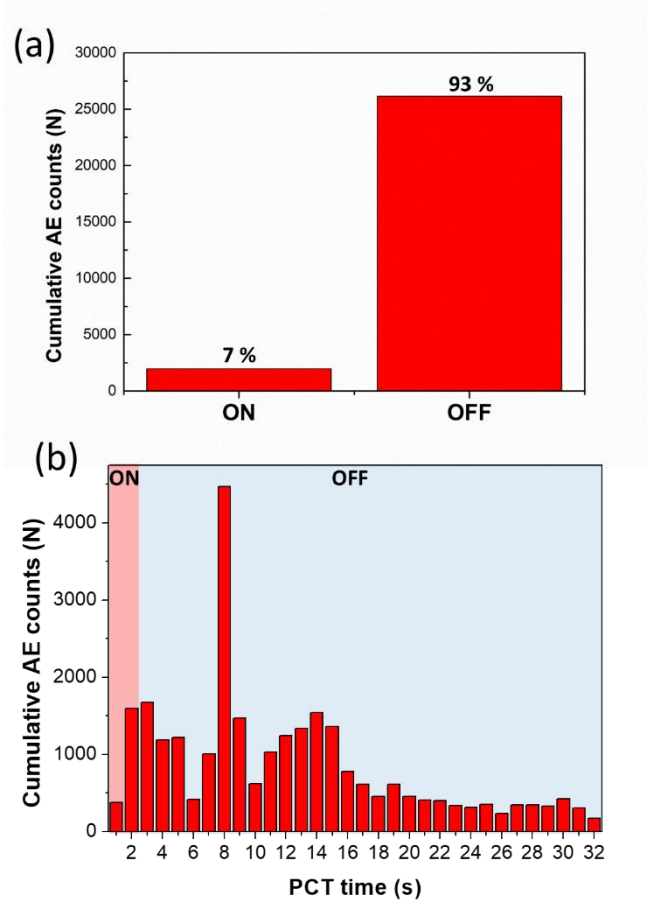


Fig. 16 (a) cumulative counts of collected AE signals during switching ON and OFF period of PCT and (b) cumulative AE counts according to cycling time of PCT test.

total AE counts) increased at a different count rate during the PCT. The count rate represents the increasing speed of the AE signal counts in unit cycle, and this is equivalent to the inclination angle of the count curve shown in Fig. 14 (a). The increase in total AE counts proceeded through three stages based on the count rate. Total AE counts steeply increased with a high-count rate initially (stage 1), then increased smoothly with a low count rate (stage 2), and was followed by an abrupt increase (stage 3). The AE counts are generally considered to optimally reflect material damage. The total AE counts were proportional to the progress of material damage wherein the damage corresponded to the AE source. Thus, the results indicate that fatigue cracks propagated based on three stages at a different rate during PCT.

To clearly divide the progress of fatigue based on the AE count stage, an AE count rate was calculated as the total count number per cycle, as shown in Fig. 14 (b). The change in the count rate clearly indicates that the progress of fatigue crack is divided into three stages as indicated by a red dashed line. The three stages can be classified into the highest count rate during the early step of PCT (stage 1), low count rate (stage 2), and re-high-count rate (stage 3). Stage 2 and stage 3 were divided at approximately 4,060 cycles where the count rate started to increase again. In fatigue tests of bulk metals, high AE count

rates were observed when fatigue cracks were initiated, cracks were rapidly propagated, and metals were finally fractured [19][48][49][50]. Based on the results of the aforementioned previous studies, stage 1 is attributed to crack initiation, as shown in Fig. 9 (c). Specifically, AE signals in stage 2 occur from the crack extension at the crack tip during the crack propagation, as shown in Fig. 9 (d). In stage 3, crack propagation caused catastrophic fractures and increased the AE count rate. Based on the relationship between the AE count rate and fatigue progress, it was concluded that AE offers the ability to accurately detect fatigue crack initiation, crack propagation, and catastrophic fracture. It demonstrated that the monitoring of the AE count rate can provide an early warning before final lift-off fracture via evaluating the progress status of fatigue cracks. The early warning could be provided when AE count rate increased more than the determined level, which indicating that the power device reaches the accelerated stage of fatigue crack propagation before final lift-off failure.

Fig. 15 shows the variation in the amplitude of collected signals during power cycling. One dot denotes the amplitude of one AE signal, and many AE signals with amplitude ranging from 30 dB to 71 dB occurred prior to lift-off failure. Low amplitude signals below 40 dB occurred throughout the whole process of fatigue damage although high amplitude signals ranging from 41 to 71 dB were emitted in the early and middle stages of total power cycling. In a bulk metal, it was reported that high amplitude signals are generated due to plastic activities ahead of a crack tip when fatigue cracks initiate and rapidly propagate [51][52][53]. Thus, high amplitude signals in stage 1 occurred due to crack initiation in Al ribbons and those in stage 2 were attributed to the accelerated crack propagation before ribbon's lift-off failure. Hence, the observations support the relationship between AE count rate and fatigue progress.

Fig. 16(a) shows the cumulative counts of collected AE signals during switching ON and OFF period in PCT. The number of cumulative AE counts during the ON period of power cycling, which is defined as the total amount of fatigue crack initiation and propagation, was significantly lower than that during the OFF period. The AE occurrence suggested that fatigue cracks of Al ribbon bonding almost nucleated and grew during the cooling stage in power cycling. Fig. 16 (b) shows the cumulative AE counts according to cycling time during PCT test in a detail. The cracking takes place more during the cooling period. In addition, the AE counts increased in the certain temperature range (at 8s) and decreased when the temperature significantly reduced (after 20s) during cooling period. This indicated that more AE counts were caused not just because of longer time. Although a detail experiment or simulation need to support, the fatigue crack looks more easily extended during the cooling process, which may be related with the change of thermal stress direction and distribution in the certain temperature range during cooling period. Recently, it was reported while the Al alloy was obviously damaged, a fast stress relief was evidenced after unloading from the tension, especially at the beginning of unloading [54]. In this study, we proposed that the cooling period lead to a fast stress relief generated at the heating period, and then leads to many cracks generation.

## V. CONCLUSIONS

The study examines the application of AE monitoring, and the results indicate detection of the progress of failure in power discrete SiC-SBD devices during power cycling tests.

Various sources of AE noise including power switching noise were completely eliminated via a noise filtering process that utilized specially designed blank specimens. A number of AE signals were successfully detected during PCT prior to reaching final failure. A physics-of-failure analysis was performed, and the initiation and propagation of fatigue cracks in Al ribbons bonding were observed although thermal damage was absent in Ag sinter joints. The source of AE signals is attributed to the initiation and propagation of fatigue cracks in Al ribbons. This demonstrates that AE monitoring exhibits excellent sensitivity to fatigue cracks. The AE acquisition can be used as a sensitive early warning method via detecting fatigue cracks that lead to catastrophic lift-off failure in the ribbons.

The variation in AE count rates, one of the parameters of AE signals, was divided into three stages, which was highly correlated with the three-step process of fatigue crack accelerated propagation observed in Al ribbon bonding, and it is defined as initiation, propagation, and catastrophic lift-off fracture. The amplitude of collected AE signals supports the correlation between the AE activities and fatigue process. Thus, it is concluded that AE monitoring can be used as an early warning method via detecting accelerated propagation stage that lead to lift-off fracture in the ribbons before catastrophic failure.

The proposed AE monitoring method in this study still has the limitation for applying to actual power modules. Sensitivity of AE sensors strongly depends on the attachment pressure and it is difficult to control it. Additionally, AE system including sensor and acquisition circuit is no price competitiveness. However, the limitation would be solved by packaging small and cheap piezoelectric elements on substrate inside power module. Future studies will focus on development of AE monitoring system using the packaged piezoelectric element inside power module to ensure reproducibility and price competitiveness.

## REFERENCES


[1] X. She, A. Q. Huang, and B. Ozpineci, "Review of Silicon Carbide Power Devices and," IEEE Trans. Ind. Electron., vol. 64, no. 10, pp. 8193–8205, 2017.

[2] J. Millan, P. Godignon, X. Perpina, A. Perez-Tomas, and J. Rebollo, "A survey of wide bandgap power semiconductor devices," IEEE Trans. Power Electron., vol. 29, no. 5, pp. 2155–2163, 2014.

[3] J. Biela, M. Schweizer, S. Waffler, and J. W. Kolar, "SiC versus Si - Evaluation of potentials for performance improvement of inverter and DCDC converter systems by SiC power semiconductors," IEEE Trans. Ind. Electron., vol. 58, no. 7, pp. 2872–2882, 2011.

[4] M. R. Werner and W. R. Fahrner, "Review on materials, microsensors, systems, and devices for high-temperature and harsh-environment applications," IEEE Trans. Ind. Electron., vol. 48, no. 2, pp. 249–257, 2001.

[5] P. Diaz Reigosa, H. Luo, and F. Iannuzzo Ge, "Implications of Ageing through Power Cycling on the Short Circuit Robustness of 1.2-kV SiC MOSFETs," IEEE Trans. Power Electron., vol. 8993, no. c, pp. 1–1, 2019.

[6] P. Ning et al., "SiC Wirebond Multichip Phase-Leg Module Packaging Design and Testing for Harsh Environment," IEEE Trans. Power Electron., vol. 25, no. 1, pp. 16–23, 2010.

[7] R. Khazaka, L. Mendizabal, D. Henry, and R. Hanna, "Survey of high-temperature reliability of power electronics packaging components," IEEE Trans. Power Electron., vol. 30, no. 5, pp. 2456–2464, 2015.

[8] S. Fu, Y. Mei, X. Li, C. Ma, and G. Q. Lu, "Reliability evaluation of multichip phase-leg IGBT modules using pressureless sintering of nanosilver paste by power cycling tests," IEEE Trans. Power Electron., vol. 32, no. 8, pp. 6049–6058, 2017.

[9] S. H. Tran et al., "Constant Δt j power cycling strategy in DC mode for top-metal and bond-wire contacts degradation investigations," IEEE Trans. Power Electron., vol. 34, no. 3, pp. 2171–2180, 2019.

[10] C. Durand, M. Klingler, M. Bigerelle, and D. Coutellier, "Solder fatigue failures in a new designed power module under power cycling," Microelectron. Reliab., vol. 66, pp. 122–133, 2016.

[11] V. N. Popok, K. B. Pedersen, P. K. Kristensen, and K. Pedersen, "Comprehensive physical analysis of bond wire interfaces in power modules," Microelectron. Reliab., vol. 58, pp. 58–64, 2016.

[12] N. Patil, J. Celaya, D. Das, K. Goebel, and M. Pecht, "Precursor parameter identification for insulated gate bipolar transistor (IGBT) prognostics," IEEE Trans. Reliab., vol. 58, no. 2, pp. 271–276, 2009.

[13] A. Hanif, Y. Yu, D. Devoto, and F. Khan, "A comprehensive review toward the state-of-the-art in failure and lifetime predictions of power electronic devices," IEEE Trans. Power Electron., vol. 34, no. 5, pp. 4729–4746, 2019.

[14] H. Oh, B. Han, P. McCluskey, C. Han, and B. D. Youn, "Physics-of-failure, condition monitoring, and prognostics of insulated gate bipolar transistor modules: A review," IEEE Trans. Power Electron., vol. 30, no. 5, pp. 2413–2426, 2015.

[15] U. M. Choi, F. Blaabjerg, and S. Jørgensen, "Power cycling test methods for reliability assessment of power device modules in respect to temperature stress," IEEE Trans. Power Electron., vol. 33, no. 3, pp. 2531–2551, 2018.

[16] A. Lahyani, P. Venet, G. Grellet, and P. J. Viverge, "Failure prediction of electrolytic capacitors during operation of a switchmode power supply," IEEE Trans. Power Electron., vol. 13, no. 6, pp. 1199–1207, 1998.

[17] H. Huang and P. A. Mawby, "A lifetime estimation technique for voltage source inverters," IEEE Trans. Power Electron., vol. 28, no. 8, pp. 4113–4119, 2013.

[18] U.-M. Choi, F. Blaabjerg, S. Jorgensen, M.-N. Stig, and R. Bjorn, "Reliability improvement of power converters by means of condition monitoring of IGBT modules," IEEE Trans. Power Electron., vol. 32, no. 10, pp. 7990–7997, 2017.

[19] D. H. Kohn, P. Ducheyne, and J. Awerbuch, "Acoustic emission during fatigue of Ti-6Al-4V: Incipient fatigue crack detection limits and generalized data analysis methodology," J. Mater. Sci., vol. 27, no. 12, pp. 3133–3142, 1992.

[20] C.-Y. Choe, W.-S. Jung, and J.-W. Byeon, "Damage evaluation in lithium cobalt oxide/carbon electrodes of secondary battery by acoustic emission monitoring," Mater. Trans., vol. 56, no. 2, pp. 269–273, 2015.

[21] S. Levikari, T. J. Karkkainen, C. Andersson, J. Tamminen, and P. Silventoinen, "Acoustic phenomena in damaged ceramic capacitors," IEEE Trans. Ind. Electron., vol. 65, no. 1, pp. 570–577, 2018.

[22] B. Legros, P. X. Thivel, Y. Bultel, M. Boinet, and R. P. Nogueira, "Acoustic emission: Towards a real-time diagnosis technique for Proton exchange membrane fuel cell operation," J. Power Sources, vol. 195, no. 24, pp. 8124–8133, 2010.

[23] T. J. Karkkainen et al., "Acoustic emission in power semiconductor modules-First observations," IEEE Trans. Power Electron., vol. 29, no. 11, pp. 6081–6086, 2014.

[24] C. Choe, C. Chen, and S. Noh, "Thermal shock performance of DBA / AMB substrates plated by Ni and Ni–P layers for high-temperature applications of power device modules," Materials (Basel)., vol. 11, pp. 2394-1–13, 2018.

[25] R. Khazaka, L. Mendizabal, D. Henry, and R. Hanna, "Survey of high-temperature reliability of power electronics packaging components," IEEE Trans. Power Electron., vol. 30, no. 5, pp. 2456–2464, 2015.

[26] K. Suganuma, S. Sakamoto, N. Kagami, D. Wakuda, K. S. Kim, and M. Nogi, "Low-temperature low-pressure die attach with hybrid silver particle paste," Microelectron. Reliab., vol. 52, no. 2, pp. 375–380, 2012.

[27] J. Dai, J. Li, P. Agyakwa, M. Corfield, and C. M. Johnson, "Comparative thermal and structural characterization of sintered nano-silver and high-lead solder die attachments during power cycling," IEEE Trans. Device Mater. Reliab., vol. 18, no. 2, pp. 256–265, 2018.

[28] F. Yu, J. Cui, Z. Zhou, K. Fang, R. W. Johnson, and M. C. Hamilton, "Reliability of Ag sintering for power semiconductor Die attach in high-temperature applications," IEEE Trans. Power Electron., vol. 32, no. 9, pp. 7083–7095, 2017.

[29] S. Park, S. Nagao, T. Sugahara, and K. Suganuma, "Mechanical stabilities of ultrasonic Al ribbon bonding on electroless nickel immersion gold finished Cu substrates," Jpn. J. Appl. Phys., vol. 53, no. 4, 2014.

[30] M. Held, P. Jacob, G. Nicoletti, P. Scacco, and M.-. Poech, "Fast power cycling test of IGBT modules in traction application," in Proceedings of Second International Conference on Power Electronics and Drive Systems, vol. 1, pp. 425–430, 1997.

[31] JEDEC JESD 51-1 Integrated circuit thermal measurement method - electrical test method (single semiconductor device). 1995.

[32] C. Durand, M. Klingler, D. Coutellier, and H. Naceur, "Power cycling reliability of power module: A survey," IEEE Trans. Device Mater. Reliab., vol. 16, no. 1, pp. 80–97, 2016.

[33] C.K. Bhagat, C.K. Mukhopadhyay, B. Purna Chandra Rao, "Design and Development of Signal Conditioning Unit for Acquisition of Acoustic Emission Signal for Metallic Materials," Trans Indian Inst Met, vol. 71, pp. 1913–1918, 2018.

[34] N.S.Mohd Jaafar, I.A. Aziz, J. Jaafar, A.K. Mahmood, "An Approach of Filtering to Select IMFs of EEMD in Signal Processing for Acoustic Emission [AE] Sensors," Advances in Intelligent Systems and Computing, vol 860, pp. 100–111, 2019.

[35] J. A. Pascoe, D. S. Zarouchas, R. C. Alderliesten, and R. Benedictus, "Using acoustic emission to understand fatigue crack growth within a single load cycle," Eng. Fract. Mech., vol. 194, no. March, pp. 281–300, 2018.

[36] K. Rhodes, N. Dudney, E. Lara-Curzio, and C. Daniel, "Understanding the degradation of silicon electrodes for lithium-ion batteries using acoustic emission," J. Electrochem. Soc., vol. 157, no. 12, p. A1354, 2010.

[37] C. Buttay, C. Raynaud, H. Morel, M. Lazar, G. Civrac, and D. Bergogne, "High-temperature behavior of SiC power diodes," Proc. 2011 14th Eur. Conf. Power Electron. Appl. EPE 2011, no. October, pp. 0–9, 2011.

[38] S. Dusmez, H. Duran, and B. Akin, "Remaining useful lifetime estimation for thermally stressed power MOSFETs based on on-state resistance variation," IEEE Trans. Ind. Appl., vol. 52, no. 3, pp. 2554–2563, 2016.

[39] K. S. Siow and Y. T. Lin, "Identifying the development state of sintered silver (Ag) as bonding material in microelectronic packaging via a patent landscape study," J. Electron. Packag., vol. 138, no. c, pp. 1–18, 2016.

[40] C. Chen, C. Choe, Z. Zhang, D. Kim, and K. Suganuma, "Low-stress design of bonding structure and its thermal shock performance (− 50 to 250 °C) in SiC/DBC power die-attached modules," J. Mater. Sci. Mater. Electron., vol. 29, no. 16, pp. 14335–14346, 2018.

[41] C. Weber, M. Hutter, S. Schmitz, and K. D. Lang, "Dependency of the porosity and the layer thickness on the reliability of Ag sintered joints during active power cycling," Proc. - Electron. Components Technol. Conf., vol. 2015-July, pp. 1866–1873, 2015.

[42] A. Alghassi, S. Perinpanayagam, M. Samie, and T. Sreenuch, "Computationally efficient, real-time, and embeddable prognostic techniques for power electronics," IEEE Trans. Power Electron., vol. 30, no. 5, pp. 2623–2634, 2015.

[43] P. D. Reigosa, H. Wang, Y. Yang, and F. Blaabjerg, "Prediction of bond wire fatigue of IGBTs in a PV inverter under a long-term operation," IEEE Trans. Power Electron., vol. 31, no. 10, pp. 7171–7182, 2016.

[44] K. Ma, U. Choi, and F. Blaabjerg GAE, "Prediction and validation of cumulative distribution function for power semiconductor devices with mission profiles in motor drive application," IEEE Trans. Power Electron., vol. 33, no. 11, pp. 9843–9853, 2018.

[45] A. K. Rao, "Acoustic emission and signal analysis," Def. Sci. J., vol. 40, no. 1, pp. 55–70, 1990.

[46] D. G. Aggelis and T. E. Matikas, "Effect of plate wave dispersion on the acoustic emission parameters in metals," Comput. Struct., vol. 98–99, pp. 17–22, 2012.

[47] P. J. de Groot, P. A. M. Wijnen, and R. B. F. Janssen, “Real-time frequency determination of acoustic emission for different fracture mechanisms in carbon/epoxy composites,” Compos. Sci. Technol., vol. 55, no. 4, pp. 405–412, 1995.
[48] C. M. Scala and S. M. K. Cousland, “Acoustic emission during fatigue crack propagation in the aluminium alloys 2024 and 2124,” Mater. Sci. Eng., vol. 61, no. 3, pp. 211–218, 1983.
[49] Z. Han, H. Luo, Y. Zhang, and J. Cao, “Effects of micro-structure on fatigue crack propagation and acoustic emission behaviors in a micro-alloyed steel,” Mater. Sci. Eng. A, vol. 559, pp. 534–542, 2013.
[50] W. G. Clark, “Fracture mechanics in fatigue,” Exp. Mech., vol. 11, no. 9, pp. 421–428, 1971.
[51] V. Moorthy, T. Jayakumar, and B. Raj, “Influence of microstructure on acoustic emission behavior during stage 2 fatigue crack growth in solution annealed, thermally aged and weld specimens of AISI type 316 stainless steel,” Mater. Sci. Eng. A, vol. 212, no. 2, pp. 273–280, 1996.
[52] C. K. Mukhopadhyay, G. Sasikala, T. Jayakumar, and B. Raj, “Acoustic emission during fracture toughness tests of SA333 Gr.6 steel,” Eng. Fract. Mech., vol. 96, pp. 294–306, 2012.
[53] M. Chai, Z. Zhang, and Q. Duan, “A new qualitative acoustic emission parameter based on Shannon’s entropy for damage monitoring,” Mech. Syst. Signal Process., vol. 100, pp. 617–629, 2018.
[54] Q. Xie, J. Lian, J.J. Sidor, F. Sun, X. Yan, C. Chen, T.K. Liu, W. Chen, P. Yang, K. An, Y.D. Wang, "Crystallographic orientation and spatially resolved damage in a dispersion-hardened Al alloy", Acta Mater, Vol. 193, pp. 138-150, 2020.